

Coordinated Planning of Synchronous Condensers and Energy Storage for Stability Enhancement in High IBR-Penetrated Systems

Zhongda Chu, Fei Teng*

Imperial College London, Department of Electrical and Electronic Engineering, London, SW7 2AZ, UK

ARTICLE INFO

Keywords:

system planning
synchronous condenser
energy storage systems
short-circuit current

ABSTRACT

Security and stability challenges in future power systems with high penetration Inverter-Based Resources (IBR) have been anticipated as the main barrier to decarbonization. Grid-following IBRs may become unstable under small disturbances in weak grids, while, during transient processes, system stability and protection may be jeopardized due to the lack of sufficient Short-Circuit Current (SCC). To solve these challenges and achieve decarbonization, the future system has to be carefully planned. However, it remains unclear how both small-signal and transient processes can be considered during the system planning stage. In this context, this paper proposes a coordinate planning model of Synchronous Condensers (SCs) and Energy Storage Systems (ESSs), both of which play a vital role in supporting small-signal and transient stability. The system strength and SCC constraints are analytically derived by considering the different characteristics of SCs and IBRs, which are further effectively linearized through a novel data-driven approach, where an active sampling method is proposed to generate a representative data set. The significant economic value of the proposed coordinated planning framework in both system asset investment and system operation is demonstrated through detailed case studies.

1. Introduction

Wide deployment of Inverter-Based Resources (IBR) has been witnessed in the past few decades, to achieve decarbonization targets [1] and energy independence across the world. Clean and sustainable as renewable energy is, it renders stability and security issues in power systems, because of its power electronic interface with the grid. Undesired events on system and area levels have been reported due to the decline of system inertia, grid strength, and voltage support, which are conventionally provided by Synchronous Generators (SGs). To further increase the IBR penetration level in the future grids while ensuring stable and secure system operation, the future grids must be carefully planned, given the stability issues due to the high IBR penetration. Furthermore, both the small-signal and transient processes can be unstable in a high IBR-penetrated system, which needs to be considered simultaneously.


Interfaced with the grid through Phase-Locked Loop (PLL), Grid-Following (GFL) IBRs suffer from small-signal stability issues in weak grids [2]. Approaches have been proposed to assess and improve the GFL stability. The dynamic modeling and stability analysis in interconnected microgrids with high IBR penetration are thoroughly reviewed in [2]. Reference [3] proposes a domain-enriched optimization algorithm to enhance the small-signal stability and dynamic resilience of islanded microgrids. The authors in [4] propose a matrix variables based modeling method for the dynamic modeling and stability analysis of distributed PV grid-connected systems.

Although novel control strategies are proposed on the IBR device level, sufficient system strength for small-signal stability maintenance should also be ensured, especially at the Point of Common Coupling (PCC) of GFL IBR, at the planning stage by optimally coordinating different resources in the system. A high-level overview of the system strength from the perspective of system planning in the National Electricity Market (NEM) grid of Australia is provided in [5], which covers the definition, attributes, and manifestations, as well as industry commentary of system strength. Two key elements that are typically considered during the planning stage to enhance the system strength are SCs and ESSs.

The authors in [6] propose an optimal allocation and sizing method to determine the sizing and allocation of SCs to minimize their installation, maintenance, and operation costs while maintaining a certain system strength at points of connection. However, the optimization is solved by meta-heuristic approaches, whose global optimality cannot be guaranteed. This issue is further addressed by the same authors in [7] by formulating the optimization model as a mixed-integer convex problem. An optimization algorithm is presented in [8] to enhance the system strength in wind-dominated power systems by allocating SCs while considering their long-term economic profitability.

Due to the voltage source nature, ESSs implemented with Grid-Forming (GFM) control are also demonstrated to be helpful in enhancing the system strength and thus the PLL-induced instability [9]. The role of Battery Energy Storage Systems (BESSs) in mitigating the voltage and frequency stability issues are investigated in [10], where a novel hierarchical optimal control framework is proposed by coordinating active and reactive power injection from BESSs. The work in [11] proposes a real-time co-simulated

*Corresponding author

 z.chu18@imperial.ac.uk (Z. Chu); F.Teng@imperial.ac.uk (F. Teng)

framework to experimentally validate the feasibility, accuracy and effectiveness of the BESS voltage and frequency support.

On the other hand, during the transient process, with limited fault levels in the system due to the retirement of SGs, system protection, and transient stability are also compromised. Fault levels at critical nodes should always be maintained above a level so that the protection devices can be triggered properly and the voltage drops across the network during a fault do not cause the extensive trip of any other major electrical components such as SGs. An optimization model to retrofit the outdated thermal units into SCs is proposed in [12] to improve transient stability, which is solved through iteration. The authors in [13] present a nonlinear optimization model to determine the optimal capacity of synchronous condensers for transient voltage stability improvement. The approaches for cost-effective investment planning which consider the effect of voltage stability in weak grids are reviewed in [14]. An optimization model for efficient allocation of BESS in power systems with high IBR penetration is presented in [15] to maximize the average voltage during faults by increasing the system strength for a set of critical scenarios. Reference [16] investigates the optimal capacity and location of BESSs in a distribution to increase the stability and reliability of power systems measured by the short-term voltage stability index. Moreover, although it is generally agreed that the contribution of BESS on the fault current is much less than that from SGs, new technologies have also been proposed to increase the temporary overcurrent capability [17, 18], which may make them also suitable for fault current provision.

Based on the above discussion, it is clear that both SCs and energy storage systems play a crucial role in maintaining the small-signal stability of GFL IBRs measured by system strength and the fault level during the transient process. It has also been demonstrated that the SCs and energy storage devices implemented with GFM control have similar contributions to system strength during normal operation and small disturbances, whereas the former provides much more fault current than the latter [19]. However, most of the existing planning works focusing on system strength improvement do not consider the different behaviors of IBRs during small-signal and transient processes, which have to be modeled separately due to the limited overloading capability of IBRs. Moreover, though SCs seem to have better performance in supporting the system stability than BESSs, the optimal solution becomes unclear considering the power/energy shifting capability of the energy storage system [20, 21] and their enhanced overloading capability enabled by the new technologies, which requires a detailed techno-economic analysis. Furthermore, most of the planning models only minimize the total investment cost but the detailed operational cost and constraints are neglected, which may lead to suboptimal or infeasible investment schemes due to a lack of operational flexibility [22].

In this context, developing a coordinated planning model that co-optimizes the sizes and locations of the SCs and ESSs

to enhance both transient and small-signal performance in high IBR-penetrated systems is thus necessary and beneficial. Note that the frequency stability issues due to the low inertia characteristics in high IBR-penetrated systems can be resolved by IBRs with additional control loops, which has been demonstrated in extensive research, thus not being considered in this work. The key contribution of this work is identified below.

- To enhance the transient and small-signal stability, the SCC and system strength constraints are analytically derived considering the different characteristics of SCs and IBRs. To evaluate the SCC while accounting for the dependence between IBR SCC injections and their terminal voltages, an iterative algorithm is further proposed with guaranteed convergence.
- The highly nonlinear SCC and system strength constraints are effectively linearized through a novel data-driven approach where an active sampling method is proposed to generate a representative data set considering the annual operational details, which significantly improves the linearization performance.
- A coordinated system planning model including operational details is formulated as a Mixed Integer Linear Programming (MILP), to improve both small-signal and transient stability in weak grids, by co-optimizing the sizes and locations of SCs and BESSs with overloading capabilities.
- The effectiveness of the proposed coordinated planning model is demonstrated through case studies based on IEEE 39-bus system, with significant cost savings and the impact of the IBR's overload capability illustrated.

The remaining part of this paper is organized as follows. Section 2 models the SG, SC, and IBR for SCC calculation. Section 3 introduces the system strength metric considered in this work, followed by system planning model formulation in Section 4. Case studies are presented in Section 5. Finally, Section 6 concludes the paper.

2. Short Circuit Current Quantification

To enhance the transient performance, sufficient SCC should be maintained at critical locations to ensure that the protection devices can be triggered properly and the voltage drops across the network during a fault do not cause the extensive trip of any other major electrical components such as SGs. To achieve this, the SCC is analytically derived as an explicit function of the decision variables in system operation and planning stages, while considering the different characteristics of the SCC contribution from synchronous units and IBRs. Utilizing the SCC-based indices to characterize the transient stability is also common in literature, e.g., [23, 24].

2.1. Modeling of SGs and SCs

The conventional model of SGs and SCs for short current calculation is the same. Therefore, only the example of SGs is given here. An SG $g \in \mathcal{G}$ is modeled as a voltage source E_g behind a reactance X_g , which can be further converted to a current source I_g in parallel with a susceptance Y_g according to the Norton's theorem:

$$I_g = \frac{E_g}{X_g} \quad (1)$$

$$Y_g = \frac{1}{jX_g}. \quad (2)$$

Replacing the SG index $g \in \mathcal{G}$ in (2) with that of SCs $s \in \mathcal{S}$ gives the expression of the SC model. It can be observed that synchronous units influence the SCC by reshaping the system admittance matrix through Y_g and Y_s .

2.2. Modeling of IBRs

The saturation of IBR current output indicates that the model of a fixed voltage behind a reactance like an SG is inappropriate for an IBR. Instead, an IBR can be modeled as a voltage-dependent current source that injects SCC depending on its terminal voltage according to the implemented droop control.

Combining the classic SCC superposition approach with the IBR model enables the SCC calculation in a general power system with both SGs and IBRs. The SCC at a fault bus F (I_F) can be computed through KCL in the pure-fault system where the only sources are those at the IBR buses and the fault bus [25]:

$$-V_F(0) = \sum_{c \in \mathcal{C}} Z_{F\Phi(c)}(I_{fc} - I_{Lc}) + Z_{FF}I_F, \quad (3)$$

where $V_F(0)$ is the pre-fault voltage at Bus F ; Z is the system impedance matrix, which also includes the impedance from SGs and SCs as defined in Section 4.2; $\Phi(c)$ maps the IBR $c \in \mathcal{C}$ to the corresponding bus index; I_{fc} and I_{Lc} are the fault current and pre-fault load current from IBR c respectively. Rearranging (3) yields the expression of the SCC at Bus F as follows:

$$I_F = \frac{-V_F(0) - \sum_{c \in \mathcal{C}} Z_{F\Phi(c)}(I_{fc} - I_{Lc})}{Z_{FF}}. \quad (4)$$

The fault current from IBR c is injected according to its terminal voltage drop, which can be modeled as a voltage-dependent current source. The UK national grid requires a reactive current of full capacity (1.0 - 1.5 p.u.) from all IBRs when their terminal voltages drop to zero [26]. Hence, the fault current from IBR $c \in \mathcal{C}$ can be calculated as:

$$I_{fc} = -d_c \underbrace{(V_{\Phi(c)} - V_{\Phi(c)}(0))}_{\Delta V_{\Phi(c)}}, \quad (5)$$

where d_c is the reactive current droop gain; $V_{\Phi(c)}$ and $V_{\Phi(c)}(0)$ are the post-fault and pre-fault voltage at bus $\Phi(c)$.

Based on the superposition principle, the voltage drop at bus $\Phi(c)$, $\Delta V_{\Phi(c)}$ can be derived:

$$\Delta V_{\Phi(c)} = Z_{\Phi(c)\Phi(c)}(I_{fc} - I_{Lc}) + Z_{F\Phi(c)}I_F. \quad (6)$$

Equation (6) is an implicit function of $\Delta V_{\Phi(c)}$, due to the dependence of I_{fc} on $\Delta V_{\Phi(c)}$. Inserting (5) into (6) and neglecting the pre-fault load current, gives the following expression of $\Delta V_{\Phi(c)}$:

$$\Delta V_{\Phi(c)} = \frac{Z_{F\Phi(c)}I_F}{1 + d_c Z_{\Phi(c)\Phi(c)}}. \quad (7)$$

Further combine (4), (5) and (7) leading to the SCC expression at fault bus F :

$$I_F = \frac{-V_F(0) + \sum_{c \in \mathcal{C}} Z_{F\Phi(c)}I_{Lc}}{Z_{FF} - \sum_{c \in \mathcal{C}} \frac{Z_{F\Phi(c)}^2}{1/d_c + Z_{\Phi(c)\Phi(c)}}}. \quad (8)$$

After neglecting the pre-fault load current, the SCC can be constrained by a predefined limit $I_{F\lim}$:

$$|I_F| = \frac{V_F(0)}{Z_{FF} - \sum_{c \in \mathcal{C}} \frac{Z_{F\Phi(c)}^2}{1/d_c + Z_{\Phi(c)\Phi(c)}}} \geq I_{F\lim}, \quad (9)$$

where the impact of IBRs on SCC is illustrated through the reactive current droop control. Note that the above SCC expression reduces to the conventional formula, $V_F(0)/Z_{FF}$, if the SCC from IBRs is neglected, i.e., $d_c = 0$.

However, there are grid codes in other countries with different requirements regarding the fault current contribution from IBRs, such as full capacity reactive current at 0.5 p.u. terminal voltage drop [27]. The fault current from IBRs as previously defined in (5) is then modified as:

$$I_{fc} = \min \left\{ I_c^{\max}, d_c \left| \Delta V_{\Phi(c)} \right| \right\}. \quad (10)$$

In this case, a simple explicit expression of the SCC as in (8) may not be available due to the interdependence between the IBR fault currents and post-fault voltages. However, I_F can still be calculated iteratively, given the system operating conditions as demonstrated in Algorithm 1. The key idea is to initialize the IBR terminal voltages to zero (Step 2) and update the IBR current (Step 5) and then the voltage (Step 7) with the latest updated voltage drop and fault current until the error of two successive steps is smaller than a predefined limit (Step 9). The convergence of the algorithm can also be proved by applying the monotone convergence theorem since $\Delta V_{\Phi(c)}^{(k)} \leq \Delta V_{\Phi(c)}^{(k+1)}$, $\Delta V_{\Phi(c)}^{(k)} \in [-1, 0]$ and a converged $\Delta V_{\Phi(c)}^{(k)}$ implies a converged $I_F^{(k)}$.

2.3. Incorporating decision variables of the planning model

In order to embed the SCC constraint derived in (9) into the system planning problem, it is necessary to demonstrate the connection between (9) and the decision variables.

Furthermore, all quantities associated with generating units defined in previous sections are per unit values based on the capacity of their own, which also need to be converted to a global base, S_{base} . For conventional SGs, their online statuses are viewed as decision variables, to account for the operational details in the planning model. Hence, the SCC model defined in (1) and (2) are modified as follows:

$$I_g = \frac{E_g S_g}{X_g S_{\text{base}}} x_g \quad (11)$$

$$Y_g = \frac{S_g}{j X_g S_{\text{base}}} x_g, \quad (12)$$

where S_g is the capacity of synchronous generator $g \in \mathcal{G}$ and $x_g \in \{0, 1\}$ is the binary decision variable, representing its online state. Similarly, for SC $s \in \mathcal{S}$, both the capacity and location are decision variables in the planning model, which can be expressed as below:

$$I_s = \frac{E_s S_s}{X_s S_{\text{base}}} \quad (13)$$

$$Y_s = \frac{S_s}{j X_s S_{\text{base}}}. \quad (14)$$

S_s is the decision variable related to the SC's capacity and location:

$$S_s x_s \leq S_s \leq \bar{S}_s x_s \quad (15a)$$

$$\sum_{s \in \mathcal{S}} x_s \leq \bar{N}_s, \quad (15b)$$

with S_s, \bar{S}_s being the lower and upper capacity limits of the potential SC $s \in \mathcal{S}$ and $x_s \in \{0, 1\}$ the binary decision of whether the SC should be installed. \bar{N}_s is the maximum number of SCs that can be installed.

As for the IBRs, the online capacities of the GFL IBRs, $c \in \mathcal{C}_l$ are decision variables during the operation stage whereas the investment capacities of the BESSs (GFM IBRs, $c \in \mathcal{C}_m$) are decision variables during the planning stage.

Algorithm 1 Iterative calculation of SCC

- 1: Set $k = 0$ and $\varepsilon = 0$
 - 2: Initialization $\triangleright \Delta V_{\Phi(c)}^{(0)} = -1$
 - 3: **while** $\varepsilon > \epsilon$ or $k = 0$ **do**
 - 4: $k = k + 1$
 - 5: Calculate $I_{fc}^{(k-1)} = \min \left\{ I_c^{\max}, d_c \left| \Delta V_{\Phi(c)}^{(k-1)} \right| \right\}, \forall c$
 - 6: Calculate $I_F^{(k)} = f \left(I_{fc}^{(k-1)} \right)$, according to (4)
 - 7: Calculate $\Delta V_{\Phi(c)}^{(k)} = \frac{Z_{F\Phi(c)} I_F^{(k)}}{1 + d_c Z_{\Phi(c)\Phi(c)}}, \forall c$
 - 8: Compute error terms $\triangleright \varepsilon_I = \left| I_F^{(k)} - I_F^{(k-1)} \right|$
 $\triangleright \varepsilon_V = \left| \Delta V_{\Phi(c)}^{(k)} - \Delta V_{\Phi(c)}^{(k-1)} \right|$
 - 9: Determine convergence error $\triangleright \varepsilon = \varepsilon_I + \varepsilon_V$
 - 10: **end while**
 - 11: Return $I_F^{(k)}$
-

Moreover, to account for the investment of the IBR temporary overloading capability, the decisions on the BESS capacities (S'_{c_m}) and its temporary overloading capacities (S'_{c_m}) are treated differently. As a result, the IBR droop control gain $d_c, \forall c \in \mathcal{C}$ can be re-scaled as follows:

$$d_c = \begin{cases} d_0 \times \frac{S_{c_l}}{S_{\text{base}}} & \text{if } c \in \mathcal{C}_l \\ d_0 \times \frac{S'_{c_m}}{S_{\text{base}}} & \text{if } c \in \mathcal{C}_m, \end{cases} \quad (16)$$

where d_0 is the droop gain based on the IBR's own capacity and S_{c_l}, S'_{c_m} are the capacity of GFL, the temporary overloading capacity of GFM converter respectively. For GFL units, $c \in \mathcal{C}_l$, their locations, and installed capacities are fixed depending on the renewable resources, whereas for the GFM units, $c \in \mathcal{C}_m$, their locations and capacities are decision variables at the system planning stage. The temporary overloading capacity S'_{c_m} can be further expressed as:

$$S_{c_m} \leq S'_{c_m} \leq \beta S_{c_m}, \quad (17)$$

where β is the temporary overload factor. S_{c_m} is the GFM capacity during normal operation being confined by:

$$\underline{S}_{c_m} x_{c_m} \leq S_{c_m} \leq \bar{S}_{c_m} x_{c_m} \quad (18a)$$

$$\sum_{c_m \in \mathcal{C}_m} x_{c_m} \leq \bar{N}_{c_m}, \quad (18b)$$

where $\underline{S}_{c_m}, \bar{S}_{c_m}$ is the lower and upper limits of S_{c_m} , $x_{c_m} \in \{0, 1\}$ is the binary decision of whether the GFM IBR should be installed and \bar{N}_{c_m} is the maximum number of GFM IBR that can be installed. Thus far, it is clear that the commitment decisions of SGs, the investment decisions of SCs, and GFM IBRs (BESSs) including both locations and capacities influence the system SCC.

3. System Strength Assessment

In order to ensure the small-signal stability of GFL IBRs, the system strengths at their terminal buses should be kept above a certain limit. Conventionally, system strength is assessed through Short Circuit Ratio (SCR), which is a locational property, being defined as the ratio of three-phase short circuit capacity to the IBR rated power. However, as the IBR penetration increases, the effectiveness of using SCR to represent system strength becomes questionable due to the neglect of IBR interactions. As a result, extensive research has been conducted in this area to define more appropriate system strength index for IBR stability characterizing, such as weighted short circuit ratio developed by ERCOT [28], the composite short circuit ratio developed by GE [29] and the Equivalent Short Circuit Ratio (ESCR) developed in [30]. In this work, the generalized Short Circuit Ratio (gSCR) in [31] is utilized as the system strength index in the system planning model to ensure the IBR stability. The gSCR is

defined as the minimum eigenvalue of the equivalent admittance matrix, \mathbf{Y}_{eq} :

$$\text{gSCR} = \lambda_{\min}(\mathbf{Y}_{eq}) \quad (19a)$$

$$\mathbf{Y}_{eq} = \text{diag} \left(\frac{V_{\Phi(c_l)}^2}{P_{c_l}} \right) \mathbf{Y}_{red}, \quad (19b)$$

where $\text{diag} \left(\frac{V_{\Phi(c_l)}^2}{P_{c_l}} \right)$ is the diagonal matrix related to the GFL IBR terminal voltage and output power and \mathbf{Y}_{red} is the reduced node admittance matrix after eliminating passive buses. It has been revealed that the smallest eigenvalue of \mathbf{Y}_{eq} represents the connectivity of the network, and thus the grid voltage strength. Different from the impedance matrix \mathbf{Z} used for SCC calculation, which includes the contribution from SGs and SCs, the admittance matrix \mathbf{Y} based on which \mathbf{Y}_{eq} in (19) is calculated, should also include the admittance of GFM IBRs as demonstrated in Section 4.2.2. This is because during the transient process (short circuit), both GFM and GFL IBRs are modeled as voltage-dependent current sources due to the saturation of inverter current, whereas for the system strength assessment, since all of the indices mentioned above are derived from the perspective of small signal stability, a GFM IBR can thus be modeled the same as a synchronous unit, i.e., a voltage source behind impedance due to its grid-forming capability [5, 32]. As a result, the system strength measured by gSCR can be enhanced by having more SG/SC and GFM IBR in the system or by reducing the output power from GFL units.

It should be noted that the focus of this work is not the derivation of the system strength index. Instead, we utilize an established index to characterize the system strength in the system planning model. Although, the specific form in (19) is chosen, the proposed method could in general deal with other system strength indices such as the composite short circuit ratio in [29] and the equivalent effective short circuit ratio in [30].

4. System Planning Problem

In this section, the proposed system planning model is mathematically formulated, where the investment of SCs, BESSs (GFM IBRs), and the temporary overloading capability of BESSs are optimally determined to maintain the required SCC level and system strength. In addition, detailed operational constraints, including the generator ramps, start-up/shut-down limits, and transmission constraints are embedded into the optimization problem to model the operational characteristics of a high IBR-penetrated system. The overall planning model is formulated as an MILP with the reformulation of the SCC and system strength constraint illustrated in this section.

4.1. Objective Function

The objective of the proposed planning model is to minimize the sum of annualized capital investment costs and the expected yearly operating cost over all nodes in a given

scenario tree:

$$\begin{aligned} \min & \sum_{s \in S} c^s S_s + \sum_{c \in C} c^c S_c + \\ & \sum_{t \in T} \sum_{n \in \mathcal{N}} \pi_n \left(\sum_{g \in \mathcal{G}} C_{t,n,g} + \Delta t \sum_{l \in \mathcal{L}} c^{VOLL} p_{t,n,l}^c \right) \end{aligned} \quad (20)$$

where c^s (or c^c) is the annualized investment cost coefficient of SC (or GFM IBR converter); π_n is the probability of scenario $n \in \mathcal{N}$ and $C_{t,n,g}$ is the operation cost of unit $g \in \mathcal{G}$ in scenario $n \in \mathcal{N}$ at time step $t \in T$ including startup, no-load and marginal cost; c^{VOLL} represents value of lost load; $p_{t,n,l}^c$ is the active power shedding of load l in scenario n at time step t . The scenario tree is built based on user-defined quantiles of the forecast error distribution to capture the uncertainty associated with demand and wind generation [33].

4.2. Short Circuit Current and System Strength Constraints

In this section, the short circuit current and system strength expressions previously explained in Section 2 and Section 3 are reformulated as linear constraints, which can be directly included in the system planning model.

4.2.1. Short circuit current constraints

Combining (9) and (16) gives the SCC constraint:

$$|I_F| = \frac{V_F(0)}{Z_{FF} - \sum_{c \in C} \frac{Z_{F\Phi(c)}^2}{S_{\text{base}}/(S_c d_0) + Z_{\Phi(c)\Phi(c)}}} \geq I_{F_{\text{lim}}}, \quad (21)$$

where $S_c = S_{c_l}$, $\forall c \in C_l$ and $S_c = S'_{c_m}$, $\forall c \in C_m$. The SCC is directly influenced by the elements in the impedance matrix \mathbf{Z} and the converter capacity S_c . The \mathbf{Z} matrix, by definition, can be obtained by taking the inverse of the system admittance matrix \mathbf{Y} as follows:

$$\mathbf{Z} = \mathbf{Y}^{-1} \quad (22a)$$

$$\mathbf{Y} = \mathbf{Y}^0 + \Delta \mathbf{Y}, \quad (22b)$$

where \mathbf{Y}^0 is the admittance matrix of the transmission lines only; $\Delta \mathbf{Y}$ denotes the additional \mathbf{Y} matrix increment due to SGs/SCs' reactance. Depending on the operating conditions of the SGs and the investment decision of SCs, the elements in $\Delta \mathbf{Y}$ can be expressed as:

$$\Delta Y_{ij} = \begin{cases} \frac{S_g}{X_g S_{\text{base}}} x_g & \text{if } i = j \wedge \exists g \in \mathcal{G}, \text{ s.t. } i = \Psi(g) \\ \frac{S_s}{X_s S_{\text{base}}} & \text{if } i = j \wedge \exists s \in \mathcal{S}, \text{ s.t. } i = \Psi(s) \\ 0 & \text{otherwise,} \end{cases} \quad (23)$$

where S_s is confined by (15) and $\Psi(\cdot)$ maps the synchronous unit $g \in \mathcal{G}/s \in \mathcal{S}$ to the corresponding bus index. It should be noted that x_g , $\forall g \in \mathcal{G}$ can be viewed as binary decision variables, whereas the SC capacity (S_s) in (23) and IBR capacity (S_c) in (21) are deemed as continuous variables, which makes (21) a highly nonlinear constraint involving matrix inverse with binary and continuous decision variables.

4.2.2. System strength constraints

Similarly, system strength constraint at GFL IBR c_l can be written as:

$$\text{gSCR} = \lambda_{\min} \left(\text{diag} \left(\frac{V_{\Phi(c_l)}^2}{P_{c_l}} \right) \mathbf{Y}_{red} \right) \geq \text{gSCR}_{\lim}, \quad (24)$$

with gSCR_{\lim} being the gSCR limit that ensures the IBR's stability. Similarly, the admittance matrix for system strength evaluation before node-reduction, \mathbf{Y} can be derived:

$$\mathbf{Y} = \mathbf{Y}^0 + \Delta \mathbf{Y}. \quad (25a)$$

During normal operation and small disturbances SGs, SCs, and GFM IBRs can be viewed as voltage sources behind impedances. Therefore, depending on the operating conditions of the SGs and the investment decision of SCs and GFM IBRs, the elements in $\Delta \mathbf{Y}$ can be expressed as:

$$\Delta \mathbf{Y}_{ij} = \begin{cases} \frac{S_g}{X_g S_{\text{base}}} x_g & \text{if } i = j \wedge \exists g \in \mathcal{G}, \text{ s.t. } i = \Psi(g) \\ \frac{S_s}{X_s S_{\text{base}}} & \text{if } i = j \wedge \exists s \in \mathcal{S}, \text{ s.t. } i = \Psi(s) \\ \frac{S_{c_m}}{X_{c_m} S_{\text{base}}} & \text{if } i = j \wedge \exists c_m \in \mathcal{C}_m, \text{ s.t. } i = \Phi(s) \\ 0 & \text{otherwise,} \end{cases} \quad (26)$$

where X_{c_m} is the GFM reactance; S_s, S_{c_m} are the planning decisions associated with SC and GFM IBR capacity, constrained by (15) and (18) respectively.

4.2.3. Constraint reformulation

As demonstrated in previous sections, the SCC and system strength constraints (21)-(26) are highly nonlinear and involve decision-dependent matrix inverse. Although it is possible to theoretically derive each element in the system impedance matrix as a function of the decision variables, the expression becomes extremely complicated in a general multi-bus system, thus being problematic to be directly included in the system planning problem. To effectively linearize the SCC and system strength constraints, the novel data-driven approach proposed in [25] is adapted. Due to the similarity of SCC and system strength constraints, only an example of the latter is presented here. First, define the linearized expression of (24):

$$\widehat{\text{gSCR}} = \sum_{g \in \mathcal{G}} k_g x_g + \sum_{s \in \mathcal{S}} k_s S_s + \sum_{c_m \in \mathcal{C}_m} k_{c_m} S_{c_m} + \sum_{c_l \in \mathcal{C}_l} k_{c_l} P_{c_l} + k_0 \geq \text{gSCR}_{\lim}, \quad (27)$$

with $\widehat{\text{gSCR}}$ being the linearized gSCR and $\mathcal{K} = \{k_g, k_s, k_{c_m}, k_{c_l}, k_0\}$ the associated linear coefficient. In order to

determine the optimal parameters \mathcal{K} , the following optimization is solved, $\forall c_l \in \mathcal{C}_l$:

$$\min_{\mathcal{K}} \sum_{\omega \in \Omega_2} \left(\text{gSCR}^{(\omega)} - \widehat{\text{gSCR}}^{(\omega)} \right)^2 \quad (28a)$$

$$\text{s.t. } \widehat{\text{gSCR}}^{(\omega)} < \text{gSCR}_{\lim}, \quad \forall \omega \in \Omega_1 \quad (28b)$$

$$\widehat{\text{gSCR}}^{(\omega)} \geq \text{gSCR}_{\lim}, \quad \forall \omega \in \Omega_3, \quad (28c)$$

with $(\cdot)^{(\omega)}$ denoting quantities associated with sample ω , and $\omega = \{x_g^{(\omega)}, S_s^{(\omega)}, S_{c_m}^{(\omega)}, P_{c_l}^{(\omega)}, \text{gSCR}^{(\omega)}\} \in \Omega$ denoting the entire data set corresponding to the gSCR constraint. It is generated by evaluating gSCR in representative system conditions. To obtain a representative data set with a finite size, a novel active sampling method is proposed in Section 4.2.4.

The sets Ω_1, Ω_2 and Ω_3 are the subsets of Ω , whose relationship is defined as below:

$$\Omega = \Omega_1 \cup \Omega_2 \cup \Omega_3 \quad (29a)$$

$$\Omega_1 = \{\omega \in \Omega \mid \text{gSCR} < \text{gSCR}_{\lim}\} \quad (29b)$$

$$\Omega_2 = \{\omega \in \Omega \mid \text{gSCR}_{\lim} \leq \text{gSCR} < \text{gSCR}_{\lim} + \nu\} \quad (29c)$$

$$\Omega_3 = \{\omega \in \Omega \mid \text{gSCR}_{\lim} + \nu \leq \text{gSCR}\}, \quad (29d)$$

with ν being a constant parameter. Given (28b) and (29b), all the data points whose real gSCR is smaller than the limit can be identified correctly by the estimated function, $\widehat{\text{gSCR}}$. Ideally, it is also desired to correctly identify all the above-limit data points, which would make the problem become a classification model. However, this may cause infeasibility due to the restricted linear structure defined in (27). Therefore, a parameter $\nu \in \mathbb{R}^+$ is introduced to define Ω_2 and Ω_3 as in (29c) and (29d). In this way, all the data points in Ω_3 will be classified correctly and misclassification can only occur in Ω_2 , thus being conservative. Furthermore, ν should be chosen as small as possible while ensuring the feasibility of (28).

4.2.4. Active Sampling

To obtain a representative data set with finite size, based on which the coefficients \mathcal{K} can be optimally determined from (28), Algorithm 2 is proposed, which is summarized as follows. Initialize \mathcal{K}^0 such that the constraint (27) becomes redundant in the first iteration ($m = 0$) and all the data points during the entire time horizon obtained by solving the planning problem \mathcal{P} are included in the set Ω^0 (Step 7 & 8). In each of the following iteration ($1 \leq m \leq m^{\max}$), solve the planning problem with the latest updated coefficients (\mathcal{K}^m) and increase the data set by $\Delta \Omega$, which includes all the data points that do not satisfy (28b) and (28c) (misclassified), as in Step 4-6 & 10. The process terminates until $\Delta \Omega = \emptyset$ or $m = m^{\max}$.

4.3. Power Balance and Power Flow Constraints

$$P_{t,n,i}^G = \sum_{\Omega_{g-i}} P_{t,n,g} + \sum_{\Omega_{w-i}} P_{t,n,w}$$

Algorithm 2 Active Sampling

```

1: Set  $m = 0$ ,  $\Delta\Omega = \{1\}$  and  $k = 0, \forall k \in \mathcal{K}^0$ 
2: Initialization  $\triangleright \mathcal{K}^0 = \{0, 0, 0, 0, \text{gSCR}_{\text{lim}}\}$ 
3: while  $m \leq m^{\max} \wedge |\Delta\Omega| > 0$  do
4:   Solve  $\mathcal{P}$  with  $\mathcal{K}^m$ , over the entire horizon  $t \in \mathcal{T}$ ,
       $\triangleright \mathbf{X}_t^m = \{x_{g,t}^*, S_{s,t}^*, S_{c_m,t}^*, P_{c_l,t}^*\}, \forall t \in \mathcal{T}$ 
5:   Calculate  $\text{gSCR}_t^m | \mathbf{X}_t^m$  and  $\widehat{\text{gSCR}}_t^m | \mathbf{X}_t^m$ 
6:   Update  $\Delta\Omega = \left\{ \mathbf{X}_t^m, \text{gSCR}_t^m | \mathbf{X}_t^m \right\}$ 
      (28b) or (28c) is violated }
7:   if  $m = 0$  then
8:      $\Omega^m = \left\{ \mathbf{X}_t^m, \text{gSCR}_t^m | \mathbf{X}_t^m \mid \forall t \in \mathcal{T} \right\}$ 
9:   else
10:     $\Omega^m = \Omega^{m-1} \cup \Delta\Omega$ 
11:   end if
12:   Solve (28) with  $\Omega^m$ ,  $\triangleright \mathcal{K}^{m+1}$ 
13:    $m = m + 1$ 
14: end while
15: Return  $\mathcal{K}^m$ 

```

$$+ \sum_{\Omega_{m-i}} p_{t,n,m} + \sum_{\Omega_{c_m-i}} p_{t,n,c_m}, \quad \forall t, n, i \quad (30a)$$

$$p_{t,n,i}^D = \sum_{\Omega_{l-i}} p_{t,n,l} - \sum_{\Omega_{l-i}} p_{t,n,l}^c, \quad \forall t, n, i \quad (30b)$$

$$p_{t,n,i}^G - p_{t,n,i}^D = \sum_{ij \in \mathcal{R}} p_{t,n,ij}, \quad \forall t, n, i \quad (30c)$$

$$p_{t,n,ij} = Y_{ij}(\theta_i - \theta_j), \quad \forall ij \in \mathcal{R}, t, n \quad (30d)$$

$$p_{t,n,ij} \leq P_{\max,ij}, \quad \forall ij \in \mathcal{R}, t, n \quad (30e)$$

Total active power generation $p_{t,n,i}^G$ and load $p_{t,n,i}^D$ at each time step t , scenario n , and bus i are defined in (30a) and (30b) with $g/w/m/c_m/l \in \Omega_{g/w/m/c_m/l-i}$ being the set of synchronous/wind/PV/storage units/loads connected to bus i . Power balance at each bus is given by (30c) to (30d) where $p_{t,n,ij}$ is power flow from bus i to j and $ij \in \mathcal{R}$ is the set of branches; Y denotes the admittance matrix of the system; $\theta_{i/j}$ is the voltage angle of bus i/j . Equation (30e) is the line rating $P_{\max,ij}$ constraint.

4.4. Thermal Unit Constraints

$$z_{1,n,g} = y_{1,n,g}, \quad \forall s, g \quad (31a)$$

$$z_{t,n,g} \geq y_{t,n,g} - y_{t-1,n,g}, \quad t > 1, \forall s, g \quad (31b)$$

$$y_{t,n,g} = y_{t-1,n,g}, \quad \forall g \in \mathcal{G}_1, t, n \quad (31c)$$

$$y_{t,n,g} p_{\min,g} \leq p_{t,n,g} \leq y_{t,n,g} p_{\max,g}, \quad \forall g, t, n \quad (31d)$$

$$-R_d \leq p_{t,n,g} - p_{t-1,n,g} \leq R_u, \quad \forall g, t \quad (31e)$$

Equations (31a) to (31c) confine generator start-up decisions ($z_{t,n,g}$) and on/off statues ($y_{t,n,g}$), where $g \in \mathcal{G}_1$ is the set of

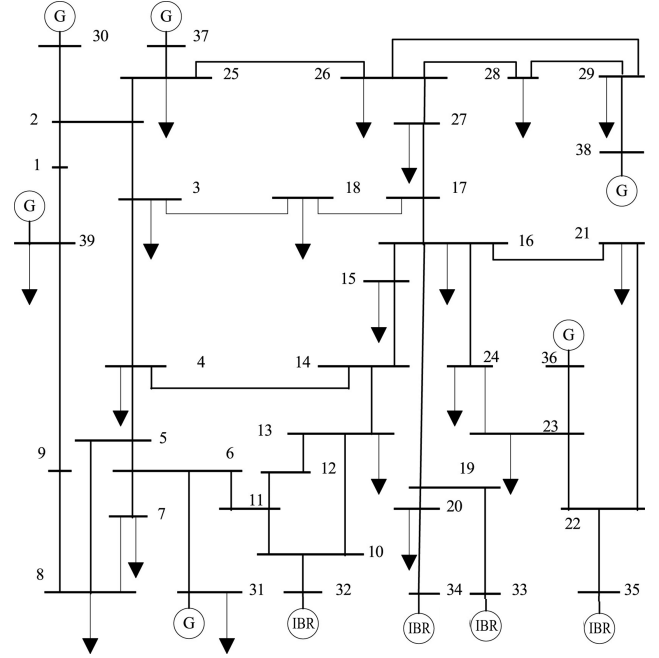


Figure 1: Modified IEEE-39 bus system.

inflexible generators.. Active power generation of thermal units, $p_{t,n,g}$ is bounded by their minimum and maximum limits ($p_{\max,g}$ and $p_{\min,g}$) as in (31d). The ramp constraint of the thermal units is considered in (31e) with R_d and R_u being the ramp down and up limits.

4.5. Constraints of battery storage system

$$p_{t,s,c_m} = p_{t,s,c_m}^{\text{dch}} - p_{t,s,c_m}^{\text{ch}}, \quad \forall t, s, c_m \quad (32a)$$

$$\bar{P}_{c_m}^{\text{ch}} \leq p_{t,s,c_m} \leq \bar{P}_{c_m}^{\text{dch}}, \quad \forall t, s, c_m \quad (32b)$$

$$\text{SoC}_{t,s,c_m} S_{c_m} = \text{SoC}_{t-1,s,c_m} S_{c_m} - \frac{1}{\eta_{c_m}} p_{t,s,c_m}^{\text{dch}} \Delta t + \eta_{c_m} p_{t,s,c_m}^{\text{ch}} \Delta t, \quad \forall t, s, c_m \quad (32c)$$

$$\text{SoC}_{\min} \leq \text{SoC}_{t,s,c_m} \leq \text{SoC}_{\max}, \quad \forall t, s, c_m \quad (32d)$$

$$\text{SoC}_{0,s,c_m} = \text{SoC}_{T,s,c_m}, \quad \forall s, c_m. \quad (32e)$$

The power injection from BESS to the microgrid (p_{t,s,c_m}) is confined in (32a) and (32b) by the upper bound of the charging ($\bar{P}_{c_m}^{\text{ch}}$) and discharging ($\bar{P}_{c_m}^{\text{dch}}$) rate. The battery state of charge (SoC_{t,s,c_m}) is quantified by (32c) with the charging/discharging efficiency η_{c_m} . (32d) imposes the upper (SoC_{\max}) and lower (SoC_{\min}) limits on the SoC of the storage devices. The SoC at the end of the considered time horizon ($t = T$) is set to be a pre-specified value equal to its initial value as in (32e).

5. Case Studies

The IEEE-39 bus system shown in Fig. 1 is utilized as the test system for constraints validation and applications. The models and parameters related to the test system are introduced in this section. To increase the renewable penetration, IBRs are added at Bus 32, 33, 34, and 35.

Table 1
Parameters of Thermal Units

Type	Type I	Type II	Type III
No-load Cost [k£/h]	4.5	3	0
Marginal Cost [£/MWh]	47	200	10
Startup Cost [k£]	10	0	N/A
Startup Time [h]	4	0	N/A
Min Up Time [h]	4	0	N/A
Min Down Time [h]	1	0	N/A
Inertia Constant [s]	6	6	6

The parameters of transmission lines and loads are available in [34]. The load and renewable generation profile in [33, 35] is adapted for the simulation during the considered time horizon. The characteristics of thermal generators are given in Table 1 while considering the data in [35, 36], with the location of the three types being Bus {30, 37}, {31, 36, 38} and {39} respectively. Other system parameters are set as follows: load demand $P^D \in [5.16, 6.24]$ GW, base power $S_B = 100$ MVA. The annualised investment costs are 1.84 k£/MVA · yr for SCs [37] and BESS for 19.88 k£/MW · yr [38, 39].

5.1. Model validations

5.1.1. SCC convergence

To demonstrate the convergence of the SCC calculation method proposed in Algorithm 1, the SCC values in each iteration are reported in Fig. 2. Note that only the SCCs at four buses selected arbitrarily are shown in the figure for clarity and those at other buses present a similar trend. It can be observed that the initial SCCs at different buses have the highest value. This is because the terminal voltages of the IBRs are initialized by $\Delta V_{\Phi(c)}^{(0)} = -1$ in Algorithm 1, thus leading to the highest current injection from IBR according to the droop control. A fast convergence of the SCC can also be observed within a few iterations, demonstrating the effectiveness of the proposed algorithm. The decreasing trend is due to the declined voltage deviation in each iteration, i.e., $|\Delta V_{\Phi(c)}^{(k)}| \geq |\Delta V_{\Phi(c)}^{(k+1)}|$.

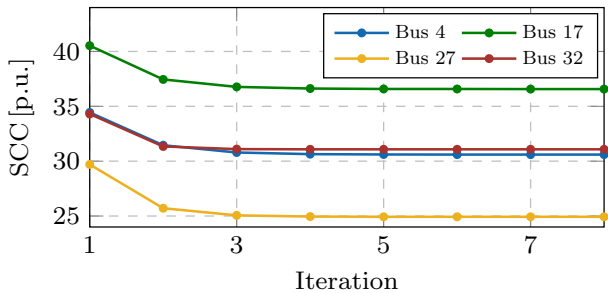


Figure 2: Convergence of SCC calculation.

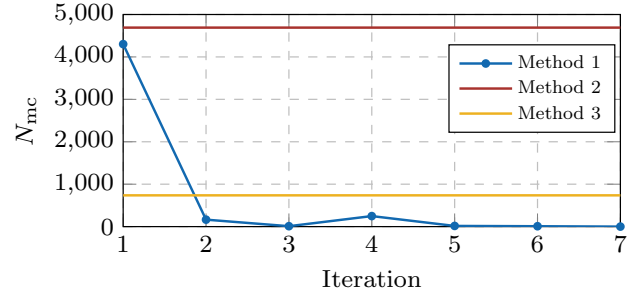


Figure 3: Convergence of active sampling.

5.1.2. Effectiveness of active sampling

The performance of constraint linearization with the active sampling algorithm as discussed in Section 4.2.3 and 4.2.4 is assessed here. The results are shown in Fig. 3 with N_{mc} being the number of misclassifications during one-year operation (8760 hours). Note that since in the proposed linearization, most of the linearized values are only required to be at the same sides as the true data samples, as defined in (28b) and (28c), the absolute errors are of no concern and not considered here.

For comparison, three different methods are considered, where Method 1 is the proposed linearization (28), with the active sampling; Method 2 is the Least Squares Regression (LSR) with random sampling; Method 3 is the proposed linearization (28), with random sampling. Methods 2 and 3 require no iteration, hence being flat curves. It can be observed from Fig. 3 that Method 2 presents the highest number of misclassifications (around half of the hours) since the LSR penalized the under- and over-estimation equally. This is improved with the proposed boundary-aware linearization approach (28), as indicated by the yellow line. However, the actual operating conditions are not considered in the sampling process, resulting in a significant number of misclassifications, which endangers system operation. As for Method 1, the number of misclassifications decreases fast within a few iterations, demonstrating the effectiveness of the proposed linearization and active sampling approach.

5.2. Benefit of BESS and SC coordinated planning

The economic benefit of coordinated planning of the BESSs and SCs is demonstrated by considering the following cases.

- Case I: Coordinated planning of BESS and SC.
- Case II: Only consider the optimal allocation of BESS.
- Case III: Only consider the optimal allocation of SC.

The system planning model of one year is solved for each case defined above. The results are listed in Table. 2 with the investment decisions and costs of both BESSs and SCs as well as the system operation cost considered. Note that the investment cost is the annualized prices whereas the system operation (Ope.) cost is the averaged hourly operational cost. In Case I, a total investment of 2.63 GW BESSs with the

Table 2
Investment and operational cost

Case	BESS Investment		SC Investment		Ope.
	Cap. [GW]	Cost [M£/yr]	Cap. [GW]	Cost [M£/yr]	Cost [k£/h]
I	2.63	52.23	0.38	0.70	165.63
II	3.96	78.68	0	0	174.94
III	0	0	1.06	1.96	440.18

cost of 52.23 M£/yr and 0.38 GW SCs with the cost of 0.70 M£/yr are needed. The BESSs are planned to provide the energy and power shifting capability to the system such that more renewable resources can be utilized. These BESSs at the same time provide a certain amount of system strength and SCC, which is however not sufficient to maintain the system requirements. Additional system strength and SCC are provided by the SCs, due to their much lower investment cost and higher SCC capacity compared with BESS.

In Case II, since only BESSs are available during the planning stage, to provide the same amount of system strength and SCC that are supplied by 0.38 GW SCs in Case I, much more BESSs (1.33 GW) at planning stage and additional SGs at operation stage are required due to the lower SCC capacity of BESSs, thus inducing more investment cost and operational cost respectively. In Case III where only the SCs are available, a lower total investment capacity of 1.06 GW is planned compared with Case I since the SCs are only needed to enhance the system strength and provide SCC. However, without any storage in the system, the operational cost is much higher than the previous two cases, as a significant amount of renewable energy is curtailed. Therefore, it is clear that the proposed approach where the BESSs and SCs can be coordinated achieves the lowest investment and operation cost.

5.3. Importance of Considering Both System Strength and SCC Constraints

The necessity of including both system strength and SCC constraints in the system planning model is demonstrated here. The results are shown in Table. 3 where three combinations of the constraints are considered with SS = 0/1 and SCC = 0/1 being to solve the planning model without/with the system strength and SCC constraints respectively. In the case where only the SCC constraint is considered, the investment decisions are very similar to the case where both constraints are included. Specifically, the decision for the SC is almost the same for the purpose of SCC provision. Slightly more BESSs are invested to decrease the operational cost. However, the system strength constraints are violated for 0.84% of the time within one-year operation. Although this number is small due to the large amount of BESS operated in GFM, it still endangers system operation. As for the case where only the system strength constraint is considered, the investment in SC is significantly reduced since the SCC is no longer enforced by the constraints. As a result, the SCC

Table 3
Impact of system strength and SCC constraints

Constraint [SS, SCC]	Investment		Violation Rate		Ope.
	BESS [GW]	SC [GW]	SS [%]	SCC [%]	Cost [k£/h]
[1,1]	2.63	0.38	0	0	165.63
[0,1]	2.72	0.36	0.84	0	163.51
[1,0]	2.64	0.02	0	54.58	135.30

constraints are violated for more than half of the time in spite of the decreased operational cost, which demonstrates the importance of including both system strength and SCC constraints in the system planning model.

5.4. Impact of wind penetration

The investment situations with various installed wind capacities in different cases are investigated in this section to demonstrate the importance of the proposed coordinated planning at different IBR penetrations. However, as the BESS is not available in Case III, the investment cost is much lower whereas the operation cost is much higher than the other cases as explained in the previous section, hence not being considered in this section. Instead, the following case is defined where the BESSs and SCs planning are decoupled, representing an optimal design of the system where the BESSs are optimally placed for power balance only and the SCs are further placed to maintain the system strength and SCC constraints given the already-determined BESSs.

- Case IV: The optimal investment of BESSs is first determined by running the planning model without the system strength and SCC requirements, which are further maintained with SCs by a second run.

The results are depicted in Fig. 4 (system operation cost) and Fig. 5 (investment cost). It is clear from Fig. 4 that as the wind capacity increases, the operation cost in all the cases decreases, since with proper amounts of BESSs in the system, the increased wind power can be effectively utilized. The operational cost in Case II is slightly higher than the other cases since more SGs are dispatched online to provide system strength and SCC due to the high investment cost

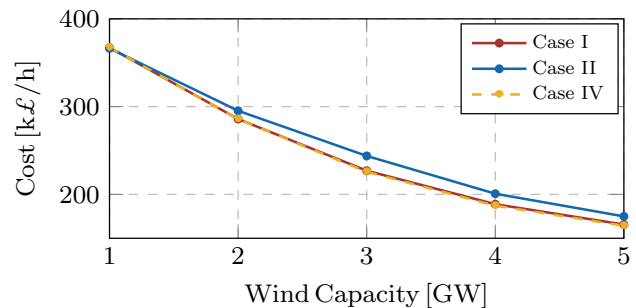


Figure 4: System operation cost with different investment strategies.

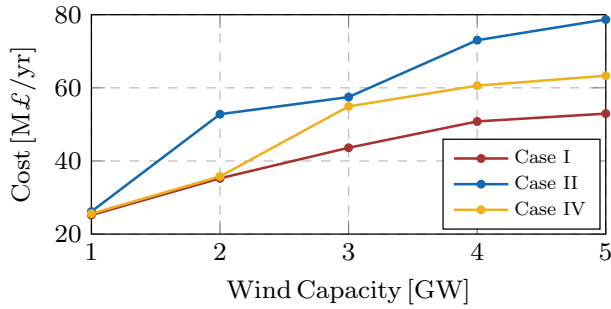


Figure 5: Investment cost with different investment strategies.

of BESSs. The operation costs in Case I and IV are almost identical to each other as they both have sufficient amounts of BESSs and SCs for power balance and system strength, SCC provision.

As for the investment cost (Fig. 5), an increasing trend can be observed along the growth of the wind capacity and Case II always presents the highest cost due to the BESS-only investment strategy. Moreover, the investment cost of Case IV becomes higher than that of the proposed method (Case I) at higher wind penetration, this is because with the decoupled planning, the BESS placement in Case IV does not consider the system strength and SCC requirement, and some redundancy in the BESS and SC capacity is resulted in, thus leading to more investment cost compared with the proposed method.

5.5. Sensitivity Analysis of IBR Overloading Capability and SCC Requirement

In previous sections, the temporary overloading capability of IBR is set as 1.2 p.u., which is much less than that of an SG/SC. As mentioned in the introduction, different approaches that can achieve a higher overloading capability of IBRs have been proposed. Therefore, the optimal planning decision may be a combination of BESS, SC, and the additional temporary overloading capability of IBRs, depending on their investment cost. However, different from the costs of BESS and SC, which are available in the literature and technical reports, the development of IBR temporary overloading capability is still in the research stage with the investment costs being unclear and varying significantly depending on the deployed technologies.

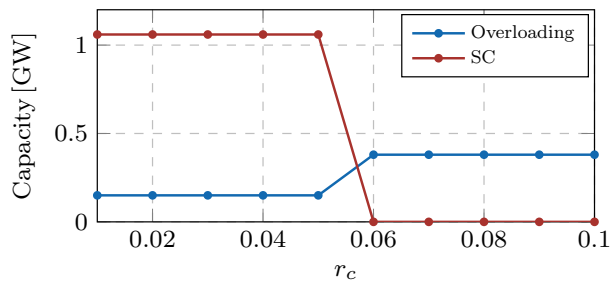


Figure 6: Investment capacity of SC and IBR overloading.

Table 4

Impact of SCC requirement levels

SCC limit factor	BESS Investment		SC Investment		Ope. Cost [k£/h]
	Cap. [GW]	Cost [M£/yr]	Cap. [GW]	Cost [M£/yr]	
1.0	2.63	52.23	0.38	0.70	165.63
1.3	2.62	52.08	1.13	2.09	165.79
1.6	2.62	52.08	2.03	3.75	165.70

Therefore, the impact of the IBR temporary overloading cost on the optimal investment decisions is investigated with the results plotted in Fig. 6 where r_c is defined as the ratio of IBR temporary overloading cost to the IBR permanent overloading cost (i.e., increasing the BESSs' converter capacity). It can be observed in the figure that when r_c is greater than 0.06, no IBR temporary overloading capacity is planned. Instead, SCs are utilized to supply SCC in the system since SCs are cheaper for the same amount of SCC provision. However, if r_c becomes smaller than 0.06, a certain amount of IBR temporary overloading capacity (1.06 GW) would be more beneficial to the system, which reduces the SC capacity from 0.38 GW to 0.15 GW. Note that the SC capacity is not reduced to zero since it also provides system strength which cannot be achieved by IBR temporary overloading. Moreover, the capacity of IBR temporary overloading required for SCC provision is much higher than the SC capacity being replaced 0.23 GW, indicating SCs provide more SCC than the IBR given the same capacity.

The impact of different levels of SCC requirements is also assessed here with the results listed in Table 4, where the SCC limit factor is the ratio of the SCC limit to that in Case I. It can be observed that compared with Case I, as the SCC limit increases, the BESS investment decisions are barely influenced, since their main roles in the system are power/energy balancing and system strength improvement. On the contrary, the invested SC capacities increase in an approximately linear fashion to maintain the increased SCC requirement, due to their superior SCC provision capability.

6. Conclusion

This paper proposes a coordinate synchronous condenser and BESS planning model for small-signal and transient stability improvement in weak grids. Sufficient system strength for small-signal stability and SCC during transient processes are ensured with minimum investment and operational costs, by optimally placing the SCs and BESSs in the system. The system strength and SCC constraints are developed considering the different characteristics of the SC and BESS. An iterative SCC calculation algorithm is proposed to account for the dependence between the IBR terminal voltage and current injection. The highly nonlinear constraints are linearized through a data-driven method where an active sampling approach is proposed to generate a representative data set.

The effectiveness of the proposed coordinated planning model is demonstrated through case studies based on IEEE 39-bus system. Less investment and operational costs are needed with the proposed method compared to the cases where only one resource is available and the case where the SC and BESS are planned separately. The value of the IBR temporary overloading capability is also investigated with the impact of the overloading cost on the optimal planning decisions being revealed.

References

- [1] R. C. Pietzcker, S. Osorio, and R. Rodrigues, "Tightening eu ets targets in line with the european green deal: Impacts on the decarbonization of the eu power sector," *Applied Energy*, vol. 293, p. 116914, 2021.
- [2] M. Naderi, Y. Khayat, Q. Shafiee, F. Blaabjerg, and H. Bevrani, "Dynamic modeling, stability analysis and control of interconnected microgrids: A review," *Applied Energy*, vol. 334, p. 120647, 2023.
- [3] J. Kweon, H. Jing, Y. Li, and V. Monga, "Small-signal stability enhancement of islanded microgrids via domain-enriched optimization," *Applied Energy*, vol. 353, p. 122172, 2024.
- [4] Q. Wang, W. Yao, J. Fang, X. Ai, J. Wen, X. Yang, H. Xie, and X. Huang, "Dynamic modeling and small signal stability analysis of distributed photovoltaic grid-connected system with large scale of panel level dc optimizers," *Applied Energy*, vol. 259, p. 114132, 2020.
- [5] L. Yu, K. Meng, W. Zhang, and Y. Zhang, "An overview of system strength challenges in australia's national electricity market grid," *Electronics*, vol. 11, no. 2, p. 224, 2022.
- [6] S. Hadavi, M. Z. Mansour, and B. Bahrani, "Optimal allocation and sizing of synchronous condensers in weak grids with increased penetration of wind and solar farms," *IEEE Journal on Emerging and Selected Topics in Circuits and Systems*, vol. 11, no. 1, pp. 199–209, 2021.
- [7] S. Hadavi, J. Saunderson, A. Mehrizi-Sani, and B. Bahrani, "A planning method for synchronous condensers in weak grids using semi-definite optimization," *IEEE Transactions on Power Systems*, vol. 38, no. 2, pp. 1632–1641, 2022.
- [8] L. Richard, T. K. Saha, W. Tushar, H. Gu *et al.*, "Optimal allocation of synchronous condensers in wind dominated power grids," *IEEE Access*, vol. 8, pp. 45 400–45 410, 2020.
- [9] X. Gong, X. Wang, and B. Cao, "On data-driven modeling and control in modern power grids stability: Survey and perspective," *Applied Energy*, vol. 350, p. 121740, 2023.
- [10] G. E. Mejia-Ruiz, M. R. A. Paternina, F. R. S. Sevilla, and P. Korba, "Fast hierarchical coordinated controller for distributed battery energy storage systems to mitigate voltage and frequency deviations," *Applied Energy*, vol. 323, p. 119622, 2022.
- [11] G. E. Mejia-Ruiz, M. R. A. Paternina, M. Ramirez-Gonzalez, F. R. S. Sevilla, and P. Korba, "Real-time co-simulation of transmission and distribution networks integrated with distributed energy resources for frequency and voltage support," *Applied Energy*, p. 121046, 2023.
- [12] J. An, J. Zhang, X. Du, C. Li, and M. Liu, "Enhance transient voltage stability by retrofitting thermal power unit to synchronous condenser," in *2022 7th Asia Conference on Power and Electrical Engineering (ACPEE)*. IEEE, 2022, pp. 1186–1192.
- [13] Y. Li, Z. Cao, Z. Zhang, B. Gao, and J. Fang, "Voltage stability index based synchronous condenser capacity configuration strategy of sending end system integrated renewable energies," in *2022 IEEE Sustainable Power and Energy Conference (iSPEC)*. IEEE, 2022, pp. 1–5.
- [14] O. B. Adewuyi, M. E. Lotfy, B. O. Akinloye, H. O. R. Howlader, T. Senjyu, and K. Narayanan, "Security-constrained optimal utility-scale solar pv investment planning for weak grids: Short reviews and techno-economic analysis," *Applied Energy*, vol. 245, pp. 16–30, 2019.
- [15] N. Cifuentes, C. Rahmann, F. Valencia, and R. Alvarez, "Network allocation of bess with voltage support capability for improving the stability of power systems," *IET Generation, Transmission & Distribution*, vol. 13, no. 6, pp. 939–949, 2019.
- [16] N.-C. Yang, Y.-C. Zhang, and E. W. Adinda, "Sizing and siting of battery energy storage systems in distribution networks with transient stability consideration," *Mathematics*, vol. 10, no. 19, p. 3420, 2022.
- [17] W. Shao, R. Wu, L. Ran, H. Jiang, P. A. Mawby, D. J. Rogers, T. C. Green, T. Coombs, K. Yardley, D. Kastha *et al.*, "A power module for grid inverter with in-built short-circuit fault current capability," *IEEE Transactions on Power Electronics*, vol. 35, no. 10, pp. 10 567–10 579, 2020.
- [18] H. Ren, W. Shao, L. Ran, G. Hao, L. Zhou, P. Mawby, and H. Jiang, "A phase change material integrated press pack power module with enhanced overcurrent capability for grid support—a study on frd," *IEEE Transactions on Industry Applications*, vol. 57, no. 4, pp. 3956–3968, 2021.
- [19] D. Lepour, M. Paolone, G. Denis, C. Cardozo, T. Prevost, and E. Guieu, "Performance assessment of synchronous condensers vs voltage source converters providing grid-forming functions," in *2021 IEEE Madrid PowerTech*. IEEE, 2021, pp. 1–6.
- [20] Y. Hu, M. Armada, and M. J. Sánchez, "Potential utilization of battery energy storage systems (bess) in the major european electricity markets," *Applied Energy*, vol. 322, p. 119512, 2022.
- [21] K. Guerra, R. Gutiérrez-Alvarez, O. J. Guerra, and P. Haro, "Opportunities for low-carbon generation and storage technologies to decarbonise the future power system," *Applied Energy*, vol. 336, p. 120828, 2023.
- [22] E. Du, N. Zhang, C. Kang, and Q. Xia, "A high-efficiency network-constrained clustered unit commitment model for power system planning studies," *IEEE Transactions on Power Systems*, vol. 34, no. 4, pp. 2498–2508, 2018.
- [23] M. Ghamasari-Yazdel, M. Esmaili, N. Amjadi, and C. Chung, "A linearized ac planning model for generations and sfcls incorporating transient stability and short-circuit constraints," *IEEE Transactions on Power Systems*, vol. 37, no. 1, pp. 715–725, 2021.
- [24] J. Machowski, P. Kacejko, S. Robak, P. Miller, and M. Wancierz, "Simplified angle and voltage stability criteria for power system planning based on the short-circuit power," *International Transactions on Electrical Energy Systems*, vol. 25, no. 11, pp. 3096–3108, 2015.
- [25] Z. Chu and F. Teng, "Short circuit current constrained uc in high ibg-penetrated power systems," *IEEE Trans. Power Syst.*, vol. 36, no. 4, pp. 3776–3785, 2021.
- [26] nationalgrid, "The grid code," UK, Tech. Rep., October 2022.
- [27] A. Q. Al-Shetwi, M. Hannan, K. P. Jern, M. Mansur, and T. Mahlia, "Grid-connected renewable energy sources: Review of the recent integration requirements and control methods," *Journal of Cleaner Production*, vol. 253, p. 119831, 2020.
- [28] J. Schmall, S.-H. Huang, Y. Li, J. Billo, J. Conto, and Y. Zhang, "Voltage stability of large-scale wind plants integrated in weak networks: An ercot case study," in *2015 IEEE Power & Energy Society General Meeting*. IEEE, 2015, pp. 1–5.
- [29] R. Fernandes, S. Achilles, and J. MacDowell, "Report to nerc erstf for composite short circuit ratio (cscr) estimation guideline," *GE Energy Consulting*, 2015.
- [30] Y.-K. Kim, G.-S. Lee, J.-S. Yoon, and S.-I. Moon, "Evaluation for maximum allowable capacity of renewable energy source considering ac system strength measures," *IEEE Transactions on Sustainable Energy*, vol. 13, no. 2, pp. 1123–1134, 2022.
- [31] W. Dong, H. Xin, D. Wu, and L. Huang, "Small signal stability analysis of multi-infeed power electronic systems based on grid strength assessment," *IEEE Transactions on Power Systems*, vol. 34, no. 2, pp. 1393–1403, 2019.
- [32] C. Yang, L. Huang, H. Xin, and P. Ju, "Placing grid-forming converters to enhance small signal stability of pll-integrated power systems," *IEEE Transactions on Power Systems*, vol. 36, no. 4, pp. 3563–3573, 2020.

- [33] A. Sturt and G. Strbac, "Efficient stochastic scheduling for simulation of wind-integrated power systems," *IEEE Transactions on Power Systems*, vol. 27, no. 1, pp. 323–334, 2012.
- [34] P. S. D. P. Committee, "Benchmark systems for small-signal stability analysis and control," Tech. Rep., August 2015.
- [35] G. Tricarico, L. S. Azuara-Grande, R. Wagle, F. Gonzalez-Longatt, M. Dicorato, G. Forte, and J. L. Rueda, "Security constrained unit commitment and economic dispatch applied to the modified ieee 39-bus system case," in *IECON 2022 – 48th Annual Conference of the IEEE Industrial Electronics Society*, 2022, pp. 1–5.
- [36] L. Badesa, F. Teng, and G. Strbac, "Conditions for regional frequency stability in power system scheduling—part ii: Application to unit commitment," *IEEE Transactions on Power Systems*, vol. 36, no. 6, pp. 5567–5577, 2021.
- [37] S. U. Mahmud, M. N. Ansary, S. R. Deeba *et al.*, "Improvement of system strength under high wind penetration: A techno-economic assessment using synchronous condenser and svc," *Energy*, vol. 246, p. 123426, 2022.
- [38] C. Augustine and N. Blair, "Storage futures study: Storage technology modeling input data report," National Renewable Energy Lab.(NREL), Golden, CO (United States), Tech. Rep., 2021.
- [39] X. Chen, Z. Liu, P. Wang, B. Li, R. Liu, L. Zhang, C. Zhao, and S. Luo, "Multi-objective optimization of battery capacity of grid-connected pv-bess system in hybrid building energy sharing community considering time-of-use tariff," *Applied Energy*, vol. 350, p. 121727, 2023.